



HAL
open science

Enhanced nanofluidic transport in activated carbon nanoconduits

Theo Emmerich, Kalangi Vasu, Antoine Niguès, Ashok Keerthi, Boya Radha, Alessandro Siria, Lydéric Bocquet

► **To cite this version:**

Theo Emmerich, Kalangi Vasu, Antoine Niguès, Ashok Keerthi, Boya Radha, et al.. Enhanced nanofluidic transport in activated carbon nanoconduits. *Nature Materials*, 2022, 21 (6), pp.696-702. 10.1038/s41563-022-01229-x . hal-03776185

HAL Id: hal-03776185

<https://hal.science/hal-03776185v1>

Submitted on 4 Oct 2022

HAL is a multi-disciplinary open access archive for the deposit and dissemination of scientific research documents, whether they are published or not. The documents may come from teaching and research institutions in France or abroad, or from public or private research centers.

L'archive ouverte pluridisciplinaire **HAL**, est destinée au dépôt et à la diffusion de documents scientifiques de niveau recherche, publiés ou non, émanant des établissements d'enseignement et de recherche français ou étrangers, des laboratoires publics ou privés.

Enhanced nanofluidic transport in activated carbon nanoconduits

Theo Emmerich¹, Kalangi S Vasu¹, Antoine Niguès¹, Ashok

Keerthi^{2,3}, Boya Radha^{2,4}, Alessandro Siria^{1,*}, Lydéric Bocquet*

¹*Laboratoire de Physique de l'École normale Supérieure, ENS, Université PSL, CNRS, Sorbonne Université, Université de Paris, 75005 Paris, France*

² *National Graphene Institute, The University of Manchester, Manchester, UK*

³*Department of Chemistry, University of Manchester,*

Manchester, UK ⁴ *Department of Physics and Astronomy,*

The University of Manchester, Manchester, UK

Carbon emerged as a unique material in nanofluidics, with reports of fast water transport, molecular ion separation, efficient osmotic energy conversion. Many of these phenomena still await proper rationalization due to lack of fundamental understanding of nanoscale ionic transport, which can only be achieved in controlled environments. Here, we develop fabrication of 'activated' two dimensional carbon nanochannels. Comparing to nanoconduits with 'pristine' graphite walls, this enables investigation of nanoscale ionic transport with unprecedented details. We show that 'activated' carbon nanochannels outperforms pristine channels by orders of magnitude in terms of surface electrification, ionic conductance, streaming current, (epi-)osmotic currents. A detailed theoretical framework allows us to attribute the enhanced ionic transport across activated carbon nanochannels to an optimal combination of high surface charge and low friction. Further, this demonstrates the unique potential of activated carbon for energy harvesting from salinity gradients with single-pore power density across activated carbon nanochannels reaching hundreds of kW/m², surpassing alternative nanomaterials.

* lyderic.bocquet@ens.fr, alessandro.siria@ens.fr

The field of nanofluidics has undergone a major leap with the recent development of artificial channels with nanoscale and subnanoscale dimensions. Advanced nanofabrication techniques have enabled the investigation of transport across one- and two- dimensional nanoconduits, unveiling a wealth of unexpected properties and unconventional molecular transport properties [1–4]. Among the investigated nanomaterials, carbon-made nanoconduits have shown exceptional properties in terms of ionic sieving, ultra-fast permeation as well as electrochemical and osmotic energy harvesting [4–15]. This peculiarity calls for further fundamental understanding of these performances. A prerequisite is to develop a nanofluidic platform with full control of the geometry and the environment, in order to disentangle the molecular physical mechanisms at play at the (sub-)nanoscales. In this context, two dimensional channels fabricated by direct van der Waals (vdW) assembly have established themselves as key tools to explore fundamental ion and water transport at the smallest scales [4]. Here, we use such 2D nanochannels to unveil the origin of the large ionic transport in carbon channels, highlighting the subtle interplay between electrification, mobile charge and hydrodynamic slippage. To this end we introduce a new route to fabricate 2D carbon nanochannels with tunable surface properties. This makes use of either electron beam induced direct etching inside an environmental scanning electron microscope (SEM) with water vapour environment or electron-beam lithography followed by reactive ion etching (RIE) with O₂ environment; see Methods section and Supplementary Information, Section 1. Once covered by a top-layer 2D material using vdW assembly, this allows fabrication of nanofluidic devices with ‘activated’ carbon surfaces. Together with the existing fabrication method for pristine carbon nanocapillaries [4], we have a comprehensive platform at our disposal to thoroughly investigate the key role of surface modifications on the nanofluidic transport on both pristine and ‘activated’ carbon surfaces, see Fig. 1.a-c. This sheds a new light on the detailed molecular mechanisms of ionic transport and show that activated carbon nanochannels outperforms pristine carbon nanochannels by orders of magnitude in terms of surface electrification, ionic conductance, streaming current, (epi-)osmotic currents, as well as osmotic energy conversion.

Characteristics and characterization of nanochannel devices

Overall, our focus in this work is to investigate surface effects – specifically surface electrification, slippage and their consequences on ionic transport –, thus we targeted channels with only moderate confinement in the range of several nanometers (from 3 to 15 nm), in contrast to previous studies with graphite channels, see *e.g.* [4, 16]. This moderate confinement allows us to disentangle surface from bulk effects in the ionic transport and characterize surface properties. Here, the studied

pristine channels with atomically smooth channel walls are 5-15 nm in height, 120-200 nm in width and a few micrometers in length, while the activated channels are 3-13 nm in depth, 100-300 nm in width and a few micrometers in length. We studied three pristine channel devices with $N=1, 30, 200$ channels; and eight activated channel devices (five were H_2O -etched and three were O_2 -etched), with $N=1,3,4$ channels; see Section 4 in Supplementary Information for the detailed geometrical aspects of the pristine channel (labeled as A, B, C) and activated channel (labeled as D-K) devices used in this work. Due to the small response, particularly for streaming measurements, the pristine channel devices are made with multiple channels. Measurements in this work are normalized to a single channel for comparison. As a result, we found minor variations in the measurements for the different devices of the same kind. For example, in view of the qualitative consistency (discussed in the later sections), normalizing the experimental data to a single channel led to minor variations in salinity dependent single channel conductivity, apparent zeta potential and extracted surface properties (surface charge and slip length) for the 3 pristine channel devices (Systems A, B and C) investigated in this work. It also applies in the case of activated nanochannel devices (Systems D-K), even though slight differences are noticed between H_2O and O_2 -etched channels (see Supplementary Information Section 3.7). Atomic force microscopy analysis shows that the H_2O -etched channel wall exhibits a relatively increased roughness of typically 0.7 to 1.1 nm r.m.s., see Fig. 1.c and Supplementary Information Section 1.3, compared to the 200 pm r.m.s. roughness of the pristine graphite crystal. In addition, Raman spectroscopy, Fig.1d, – with 350 nm lateral resolution – on the activated channels shows D-peak, representing the defects on sp^2 crystalline structure of graphite [17, 18] due to EBIE. The emergence of a D-peak has also been observed after oxygen plasma treatment of graphite[19]. Hence, the key difference between pristine and activated nanochannel is that, in pristine nanochannel both the channel walls are made of pristine graphitic surface whereas in the activated nanochannel, the bottom channel wall contains charged sites and nanometric roughness. In H_2O -etched nanochannels, we attribute this defect formation to the etching of graphitic surface with highly reactive radicals such as $OH\bullet$, $H\bullet$, and $HO_2\bullet$, created by the electron beam under water vapor atmosphere in environmental SEM [20, 21]. Further, molecular dynamics simulations have shown that water self-dissociation on graphene edges is energetically favorable[22] . Thus, the EBIE/RIE induced defects and self-dissociation of water could contribute to the high surface charge in 'activated' nanochannels – as indeed confirmed below – which governs the ionic transport across them. Our electrostatic force microscopy measurements further confirm the difference in surface charge distribution on pristine and activated graphite

surfaces (Supplementary Information Section 1.3). Chemical analysis of EBIE-made nanoscale patterns remains out of reach because of the spatial resolution of the chemical probes. Our XPS chemical analysis of millimetric-scale graphite exposed to the same RIE program used to obtain the O₂-etched nanochannels unveils an increase of oxygen and C/O species following the etching (see Supplementary Information Section 2). This is in good agreement with previous XPS analysis of O₂ and H₂O plasma exposed graphite[19, 23] and point to the presence of charged C/O groups attached to the activated channel's bottom wall.

Ionic transport under electric potential and pressure gradients

Before tackling the osmotic energy conversion across the various carbon devices, we first perform an exhaustive investigation of their ionic response and surface properties. Hence, we first explore ionic transport through pristine channels under voltage and pressure drop, Fig. 2a-d. Such experiments [under voltage drop and pressure drop] enable measuring the conductivity and electro-osmotic mobility (or apparent zeta potential) respectively. This allows us to characterize the electrokinetic properties of the system and get insights into the water-graphite and ion-graphite interfacial behavior. The pristine channels exhibit a linear dependence of the ionic current (per channel), I/N , with applied voltage ΔV (Fig. 2a) and show a strong dependence of the single channel conductivity, $K/N = \frac{L}{N.w.h} \frac{I}{\Delta V}$ (L,w,h the length, width and height of each channel) with the salt concentration, Fig. 2b. Further insights on the surface electrostatic properties are obtained by streaming current measurements, Fig. 2c, where the ionic current I_{stream} is measured as a function of an applied pressure drop ΔP . I_{stream} exhibits a linear response versus ΔP for all KCl concentrations as shown in Fig. 2c and one extracts the electro-osmotic mobility ($\mu_{EO} = \frac{L}{Nwh} \frac{I_{stream}}{\Delta P}$). The apparent zeta potential of the surface is defined using Smoluchowski expression, $\zeta_{app} = -\frac{\eta}{\epsilon\epsilon_0} \mu_{EO}$ (with η the water dynamic viscosity, ϵ the water relative permittivity, ϵ_0 the vacuum relative permittivity). Note that the Smoluchowski expression remains valid down to nanometric confinement[16]. The apparent zeta potential is used here as a phenomenological parameter quantifying electro-osmotic mobility. It is one of the few tools available for studying charged interfaces along with short interaction microscopy and spectroscopy methods[24]. The apparent zeta potential exhibits a non-monotonic dependence on the salt concentration, with relatively high values ranging between -40 and -80 mV; Fig. 2d.

Let us turn to the ionic response across the activated channels. The ionic conductivity – as obtained from the I-V characterization, Fig. 2a' – is shown in Fig. 2b'. Ionic conductivity of activated channels is found to be several orders of magnitude larger than the bulk conductivity

(solid line), as well as ionic conductivity observed for the pristine channels in Fig. 2b, furthermore with a weak dependence on the salt concentration. Such a very strong deviation from bulk effects are confirmed by streaming current measurements on the activated channel, Fig. 2c', and the corresponding apparent zeta potentials in Fig. 2d'. These measurements on activated carbon surface highlight huge values of apparent zeta potential, ranging between -0.5 to -2 V (one order higher than that of pristine graphitic surface). To the best of our knowledge, such values of apparent zeta potentials are unprecedented. Nanofluidic transport inside systems with low friction alone, such as pristine nanochannels, or high surface charge alone, such as h-BN nanochannels[16, 25] or nanotubes [26] is of lower magnitude. These behaviors are obtained for all devices with activated surfaces that we measured in the present study, see Fig. 3 for the conductivity.

Theoretical analysis of conductivity and electro-osmotic mobility

Before taking benefit of such unique properties, the previous results for both the pristine and activated carbon channels call for a proper understanding. The high conductance and electro-osmotic mobility immediately indicate considerable surface transport, however we show that a complete rationalization of our experimental data is reached only after considering the concerted role of surface electrification and hydrodynamic slippage [16, 27].

Our experimental data reporting both conductance and electro-osmotic mobility allows to disentangle both effects and provide much insight into the molecular surface mechanisms. For pristine channels, though the channel height is larger than Debye length for most experiments, the conductivity per channel for all concentrations is found to be significantly larger than the bulk conductance, $K > K_{\text{bulk}} = 2\mu e^2 C_s$ (per channel, with μ the salt bulk mobility $\mu = \frac{1}{2}(\mu_{K^+} + \mu_{Cl^-})$ [27]); $\mu = D/k_B T$ with D the diffusion coefficient and $k_B T$ the thermal energy. This is in contrast to what would be expected, as for such channel sizes, bulk effects are usually dominant at large ($\sim 1\text{M}$) concentrations. It was recently pointed out by experiments in CNTs and *ab initio* simulations [28, 29] that electrification of pristine graphite can result from physisorption of hydroxide ions on the carbon surface, with the OH^- ions keeping a large motility on the surface. The effect of surface charge mobility on the ion transport in confined channels is accounted for by the framework introduced in [16, 30], which, as a key ingredient, includes a supplementary contribution to the conductivity associated with the mobility of the surface charge of the form, $2\mu_m \frac{\Sigma_m}{h}$ with Σ_m the physisorbed charge, μ_m the surface mobility of the physisorbed ions (here, hydroxyl ions with $\mu_m \approx \mu_{\text{OH}^-}$ [28]). The effect of this mobile surface charge, as evidenced in *ab initio* simulations in [28], has not been properly appreciated up to now. Typically, hydrophobic surfaces with low

surface charge are shown to be significantly influenced by the mobile surface charge [28–30].

Our analysis is based on the transport framework introduced in [16, 30, 31] and accounting for the effects of mobile charge, hydrodynamic slippage and non-linear Poisson-Boltzmann electrostatics. For pristine graphite, we will neglect any chemisorbed surface charge. see Supplementary Information Section 4 for the summary of modeling parameters and assumptions.

$$\begin{aligned}
K_{\text{surf}} &= \frac{2}{h} \left[\mu e |\Sigma_m| (1 + \delta) \times \frac{\chi}{\sqrt{1 + \chi^2 + 1}} + \frac{b_0}{\eta} \times \frac{(1 - \alpha_{\text{ion}})^2 \Sigma_m^2}{1 + \beta_s \times \frac{|\Sigma_m|}{e} \ell_B^2} + e \mu_m |\Sigma_m| \right] \\
\mu_{EO} &= - \left[\frac{\epsilon \Psi_0}{\eta} + \frac{b_0}{\eta} \times \frac{(1 - \alpha_{\text{ion}}) \Sigma_m}{1 + \beta_s \times \frac{|\Sigma_m|}{e} \ell_B^2} \right] \\
\chi &= 2\pi \lambda_D \ell_B \frac{|\Sigma_m|}{e} = \sinh \left[\frac{-e \Psi_0}{2k_B T} \right]
\end{aligned} \tag{1}$$

where Σ_m is the charge due to mobile physisorbed OH^- ; b_0 is the slip length; $\ell_B = e^2/4\pi\epsilon k_B T$ is the Bjerrum length and $\lambda_D = (8\pi\ell_B C_s)^{-1/2}$ the Debye length with C_s the salt concentration – here in number of ions per cubic meter –; $\delta = 1/(2\pi\ell_B \mu \eta)$ (η the fluid viscosity). The parameters $\alpha_{\text{ion}} \in [0, 1]$ and β_s are dimensionless parameters [30] characterizing the differential friction of mobile ions and water molecules with other molecules with respect to the surface. As suggested by previous experiments in [16], we considered $\alpha_{\text{ion}} = 0.8$ and $\beta_s = 50$ for the present work.

The expressions in Eq.(1) account for the electro-phoretic and -osmotic contribution to transport, as well as the slippage-induced enhancement of electro-osmosis; the last term of K_{surf} accounts for the mobility of physisorbed hydroxide ions, with $\mu_m \simeq \mu_{\text{OH}^-} = 13 \times 10^{11} \text{ s.kg}^{-1}$. While one expects that such framework can only provide an approximation of the mechanisms at play, it captures all key physical ingredients here and we consider it as guide to rationalize the physics at play. For each salt concentration, one can extract the surface charge Σ_m and slip length b_0 from the combined values of the measured surface conductance $K_{\text{surf}} = K - K_{\text{bulk}}$ and electroosmotic mobility/ apparent zeta potential. This enables obtaining analytical expressions of the surface charge and slip length versus the salt concentration, with constant parameters acquired by curve fitting. They can then be used in equation 1 to predict the conductivity and apparent zeta potential (solid and dashed lines in Figure 2-3). We note that the fitting procedure for the combined conductivity and apparent zeta potential does not converge for lowest and highest concentration, corresponding to low charge/high slippage and vice-versa. Results are summarized in Supplementary Tables 1 and 2 for the pristine channels considered (at pH 5.5). We emphasize that without the contribution of mobile charge to the conductivity in Eq.(1), it is not possible to account consistently for the experimental data for the conductivity and apparent zeta potential. Interestingly the extracted charge is in the range

-(5-50) mC/m² and its concentration dependence can be described as $-\Sigma_m(C_s) = \gamma \times C_s^\alpha$ with the exponent α taking consistent values for the two pristine channels, $\alpha = 0.62$ and $\alpha = 0.68$ (C_s in mM); see Supplementary Tables 11. Such scaling laws for the surface charge was actually recently put forward, with an exponent in the range 0.3-1 [32–34]. The slip length decrease with salt concentration (and hence surface charge), with values between tens of nanometers down to 1 nm. One can conveniently describe the concentration dependence of the slip length as $b_0(C_s) = B_m/(1 + \omega C_s^\beta)$ with $B_m = 35$ nm, $\omega = 3 \times 10^{-4}$ (C_s in mM) and $\beta = 2.4$ and we will use the same expression for all pristine channels. It is noteworthy that the competing effect between the concentration dependent mobile surface charge and slip length of pristine graphitic surfaces results in non-monotonic behaviour of apparent zeta potential as a function KCl concentration for pristine nanochannels.

Now, using these expressions as inputs in Eq.(1) for the concentration dependence of the charge and slip length, one obtains prediction for the enhanced conductivity K/K_b , see Fig.3.a-b, and Supplementary Figure 11.d; as well as for the apparent zeta potential, see Fig.2d, and Supplementary Figure 10b. It shows a very good agreement for all concentrations for both the conductivity and apparent zeta potential. Importantly the mobile charge contribution dominates conductivity (with minor effect of slippage contribution), while the apparent zeta potential is very sensitive to slippage effects. That a unique expression for the slip length allows to reproduce the apparent zeta potential of different channels assesses the robustness of the description. Interestingly, the exponent α for the concentration dependence of the charge is close to 0.5, which is the expected exponent for a constant surface potential in the Debye-Hückel limit. Hence, we also report as a dashed line the predicted concentration dependence for the conductivity and apparent zeta potential using a fixed surface potential Ψ_0 , hence replacing the concentration dependence of Σ_m – (dashed line in Fig.3a and 3b and Supplementary Figures 10b-11d). The latter shows an overall very good agreement with the experimental data, suggesting that the pristine graphite may be well described by this simple constant potential framework. The values for the surface potential of the pristine carbon surfaces are typically in the range of several $k_B T/e$ (~ 25 mV) as expected for physisorption. This charging mechanism is in good agreement with our pristine channels pH measurements showing an increases of the conductivity with hydroxide ion concentration (see Section 3.6 in Supplementary Information).

Let us now turn to the results for activated carbon surfaces. The considerable enhancement of the conductivity and apparent zeta potential – see Fig. 2b',d' and Fig3.c-d (see also Supplementary Figure 10 and 11) suggests defect-induced electrification of the activated carbon surface as a dom-

inant mechanism and one can safely neglect the previous mobile charge contribution in this case. Accordingly, we use a simplified version of the previous model, with the mobile charge replaced by a fixed (chemisorbed) surface charge Σ and $\alpha_{ion} = \beta_s = 0$ for fixed charge. This considerable enhancement also indicates that the bottom wall that has been exposed to electron-beam dominates the ionic transport in the activated channel. Hence, the previous expressions should be divided by a factor of 2 to take into account the activated channel's asymmetry by neglecting the top pristine wall contribution. To verify that the enhancement is not coming from slippage induced by the top layer we fabricated a control activated channel with a slip-less h-BN top layer that also behaved as an activated channel (see Supplementary Figure 14). From the combined experimental data for the conductivity and apparent zeta potential, one can infer the surface charge and slippage. Extracted data for the various investigated systems are given in Supplementary Tables 4-5. Overall, the surface charge reaches much larger absolute values, in the range of C/m², while the slip length strongly decreases with salt concentration to reach a few Ångströms at high concentration and is typically in the range of Debye lengths. Overall, data for the various activated systems explored – with confinement between 3 and 13 nm –, are consistent with scaling behaviors $-\Sigma \propto C_s^\alpha$, and $b_0 \propto C_s^{-\beta}$ with $\alpha \in [0.32, 0.4]$ and $\beta \in [0.55, 0.6]$ (see Supplementary Tables 12 and Supplementary Information Section 4 for complete list of parameters). Interestingly the concentration dependence for the surface charge is fully consistent with a charge regulation behavior, which predicts an exponent of 1/3 [29], pointing to the chemical reactivity of the activated carbon surface. The scaling for the slip length suggests a relationship $b \sim \Sigma^{-\theta}$ with $\theta \approx 1.5 - 1.7$, which is consistent with recent predictions suggesting $\theta = 1 - 2$ depending on the regime considered [35, 36]. Using these scaling laws for the charge and slippage as only ingredients, one can now predict the functional dependence of the enhanced conductivity on salt concentration, as well as that of the apparent zeta potential: this shows a very good agreement with the experimental data for all investigated activated systems, see Fig.3.c-d (see also Supplementary Figure 10 and 11). In the end, only 4 parameters are needed to reproduce the data for the enhanced conductivity and apparent zeta potential per channels, with one parameter α being constrained to a value close to 1/3, while the others are consistent between the various activated channels. Note that in contrast to the pristine graphite, the fixed surface potential prediction is less effective for the activated channels, as shown in Fig.3.c-e using typical values for the potential ($\Psi_0 \sim -0.2V$). We further performed ionic current measurements using KCl solutions with different pH to investigate its influence on ionic conductivity and apparent zeta potential (see Section 3.6 in Supplementary Information). It appears that activated channels

have a higher sensitivity towards acidic pH in line with the chemical reactivity of carboxylic acid (-COOH).

Overall, the data for the various channels with activated graphite are qualitatively consistent between each others – notably in terms of the measured scaling laws for the charge and slip –, with furthermore a semi-quantitative agreement, with only slight differences in the quantitative values for the charges and slip lengths. For example, it is obvious from Supplementary Tables 4.1 that, regardless of the channel dimensions, the salinity dependence of conductivity enhancement and apparent zeta potential (electro-osmotic mobility) for System D and System E shows adequate consistency in terms of absolute values and scaling laws which is again well reflected from the salinity dependence of surface charge and slip length values. The similar consistency in salinity dependence of conductivity enhancement and apparent zeta potential values also applies in the case of pristine nanochannel devices System A and System B with different dimensions (Supplementary Tables 4.1). However, it is noteworthy that with the same channel height of 10 nm, for any KCl concentration the activated nanochannel device (System D) exhibits significantly high surface charge and apparent zeta potential and, considerably small slip length values compared to pristine nanochannel device (System B). Overall, the activation increases the surface charge by 1-2 orders of magnitude and reduces the slip length by one order of magnitude compared to pristine graphitic surface (Supplementary Figure 17). Considering the randomness of surface etching in EBIE and RIE methods, activated carbon surface in our work can be regarded as heterogeneously charged surface. We observe a strong decrease of the slip length with the surface charge on activated surfaces (Supplementary Figure 18). Such a behavior was recently attributed to a heterogeneous surface charge distribution[36]. Our theoretical analysis thus enables extracting effective surface properties, which average over surface inhomogeneities, as described *e.g.* by [36, 37]. A key finding is that activated carbon surfaces exhibit a unique combination of high charge with significant slip length, on the order of the confinement length scale (Supplementary Figure 19).

Ionic transport under salinity gradients

Building on these physical insights, we now turn to the ionic response under salinity gradients. We use different KCl concentrations in the two reservoirs in the range 1 – 1000 mM and measure the resulting electric current on the Ag/AgCl electrodes for a variety of concentration ratios, C_{\max}/C_{\min} , keeping the maximum concentration to 1M. Following [26, 38], the obtained current is corrected for the contribution resulting from the Nernst potential and originating in the difference in salt concentration at the two electrodes (see Supplementary Information Section 3.3).

As shown in Fig. 4, we observe a strong contrast between pristine and activated channels. Within the experimental error, no significant osmotic current is measured for pristine channels. This is in contrast to activated channels, for which a very large osmotic contribution to the current in the nanoampere range is measured for all investigated devices. We report in the inset the corresponding transport coefficient, K_{osm} , defined as $\frac{I_{\text{osm}}}{N} = \frac{w \cdot h}{L} K_{\text{osm}} \Delta \log[C_s]$. In the following, we will report this current as the 'epi-osmotic current' as it takes its root in a surface (diffusio-osmotic) contribution to the current; K_{osm} will be reported as the 'epi-osmotic mobility'. Diffusio-osmosis is the generation of a water flux occurring in the vicinity of a charged interface in the presence of a solute concentration gradient[26]. The water flux drags the Debye layer which results in the generation of an ionic "diffusio-osmotic" current. A key feature of charged nanopores promoting diffusio-osmotic current is that they do not require selectivity. Further, selectivity of such pores cannot be determined from concentration drop experiments as the fluid velocity is not neglectable. One may rationalize the epi-osmotic current using the same framework as above. According to [30], the epi-osmotic mobility is predicted as

$$K_{\text{osm}} = \left(\frac{1}{2}\right) \times \frac{-2\Sigma}{h} \frac{k_B T}{2\pi\eta\ell_B} \left(1 - \frac{\sinh^{-1}\chi}{\chi} + (1 - \alpha_{\text{ion}}) \frac{b_0}{\lambda_D} \frac{\sqrt{1 + \chi^2} - 1}{1 + \beta_s \times \frac{|\Sigma|}{e} \ell_B^2}\right) \quad (2)$$

where factor (1/2) applies to the activated surfaces only and stems from the contribution of the bottom layer only; as in the above analysis, the parameters α_{ion} and β_s are zero for the activated surface. For the pristine channels, $K_{\text{osm}} \approx 0$ within our experimental uncertainty. This is actually consistent with the predicted value for the epi-osmotic mobility for a pristine system: using Eq.(2) with previous charge and slippage yields $K_{\text{osm}} \approx 10^{-2}$ A/m, hence more than two orders of magnitude smaller than the values for the activated channels, in agreement with the experiments. This huge difference in epi-osmotic mobility between the channels can be understood from the limiting behaviors of Eq.(2), which scales as Σ for large charge but as Σ^3 for low charge (Supplementary Information Section 4.2), enhancing the differences between systems with different electrification. We use the previously obtained concentration-dependence of the charge and slip length of the various channels and report in Supplementary Fig.16 the predicted plot of the epi-osmotic mobility K_{osm} as a function of the conductivity K of the channels. The agreement between the experimental data for the activated channels and the prediction is good, even more that all parameters – for the charge and slip – were determined from the previous voltage and pressure drop measurements and in view of the sensibility of K_{osm} to small charge differences. This confirms the consistency of all measured mobilities characterizing the activated channels, conductivity, apparent zeta potential

and epi-osmotic mobility.

The maximum power generated is expressed as $P = I_{\text{osm}}^2/4G$ with G the channel conductance [26]. Those values, extracted from the concentration gradient experiments, are displayed in Fig.4b. Activated carbon nanochannels can generate almost 1 nW at maximum concentration gradient, only matched by atomically thin MOS_2 nanopore [38]. In order to get a proper sense of the performance of the activated channels in terms of osmotic power, a usual figure of merit corresponds to the generated electrical power per unit surface of the channel. The corresponding single pore power density (osmotic power per unit cross-sectional area) $P^* = \frac{P}{Nwh}$ as a function of the salinity gradient is shown in Fig. 4c. Single pore power density for activated channels can reach up to 100 kW/m^2 , which is one to few orders higher than that of measured for boron nitride nanotubes and other single pore fluidic devices [26, 39–41] and, comparable with what was obtained with atomically thin MoS_2 nanopores [38]; see comparison of single channel performances in Supplementary Table 15.

The phenomena at stake is of particular interest in the context of the energy conversion from the mixing of masses of water with different salinities. Although as much as 0.7 kWh of energy could theoretically be captured per cubic metre of water, the efficiency of energy extraction process remains as to now a fundamental and technical challenge. Here we show that harnessing epi-osmotic currents on activated carbon is a proper avenue to boost the osmotic energy harvesting from salinity gradients. The single pore figure allows to screen for novel nano-materials with enhanced performances in terms of osmotic energy conversion. One expects that further factors will affect the osmotic performance when upscaling to macroscopic membranes for large-scale production of osmotic power, such as pore density, concentration polarization and entrance resistance [42, 43]. However, the mechanism of strong electrification of graphite under electron irradiation unveils new avenues to fabricate activated carbon-based membrane at large-scale.

Acknowledgements

L.B. thanks R. Netz and B. Rotenberg for fruitful discussions. We thank the Institut des Matériaux de Paris Centre (IMPC FR2482) for servicing XPS instrumentation, as well as Dr Alex Walton for his help with XPS measurements and valuable discussions. L.B. acknowledges funding from the EU H2020 Framework Programme/ERC Advanced Grant agreement number 785911-Shadoks and ANR project Neptune. A.S. acknowledges funding from the EU H2020 Framework Programme/ERC

Starting Grant agreement number 637748-NanoSOFT. L.B. and A.S. acknowledge support from the Horizon 2020 program through Grant No. 899528- FET-OPEN-ITS-THIN. K.S.V. acknowledges Marie Curie Individual Fellowship from EU H2020 Framework Programme, through Grant No. 836434, GraFludicDevices. A.K. acknowledges Ramsay Memorial Fellowship, and also funding from Royal Society research grant RGS/R2/202036. B.R. acknowledges the Royal Society fellowship and funding from the EU H2020 Framework Programme/ERC Starting Grant number 852674 AngstroCAP. This work has received the support of *Institut Pierre-Gilles de Gennes* (program ANR-10-IDEX-0001-02 PSL and ANR-10-LABX-31). A.K. acknowledges Ramsay Memorial Fellowship and Royal Society research grant RGS/R2/202036.

Contributions

L.B. and A.S. designed and directed the project. T.E. and K.S.V. contributed equally. They fabricated devices, with inputs from A.N. and A.S.; R.B and A.K. contributed to device fabrication and characterization; T.E. and K.S.V. performed experiments and carried out analysis with inputs from L.B. and A.S.; L.B. performed theoretical analysis; L.B., K.S.V., T.E. and A.S wrote the manuscript. All authors contributed to discussions.

Competing interests

The authors declare no competing interests.

Figure Legends/Captions

Figure1. Nanofluidic 2D channels and measurement setup. a, Experimental Setup. Voltage, pressure or concentration drop are used to induce an ionic current across two different kinds of graphene 2D nanochannels. b, Pristine channels. Left : schematic, the Silicon Nitride membrane is grey, the bottom layer is black, the spacers are blue and the top layer is glassy transparent grey. Right : Atomic force microscopy image. c, Activated channels. Left : schematic, the Silicon Nitride membrane is grey, the bottom layer with a milled nanochannel is black and the top layer is glassy transparent. Middle : Atomic force microscopy image. the cross section displays limited sagging of the top layer over the bottom layer's through-hole, confirming good interlayer contact. Scale bar: 2 micrometers. Right : Atomic force microscopy zoomed image of the channel with cross section. Scale bar: 150 nanometers. d, Raman characterization of pristine graphitic surface and, activated graphitic surface created by SEM milling.

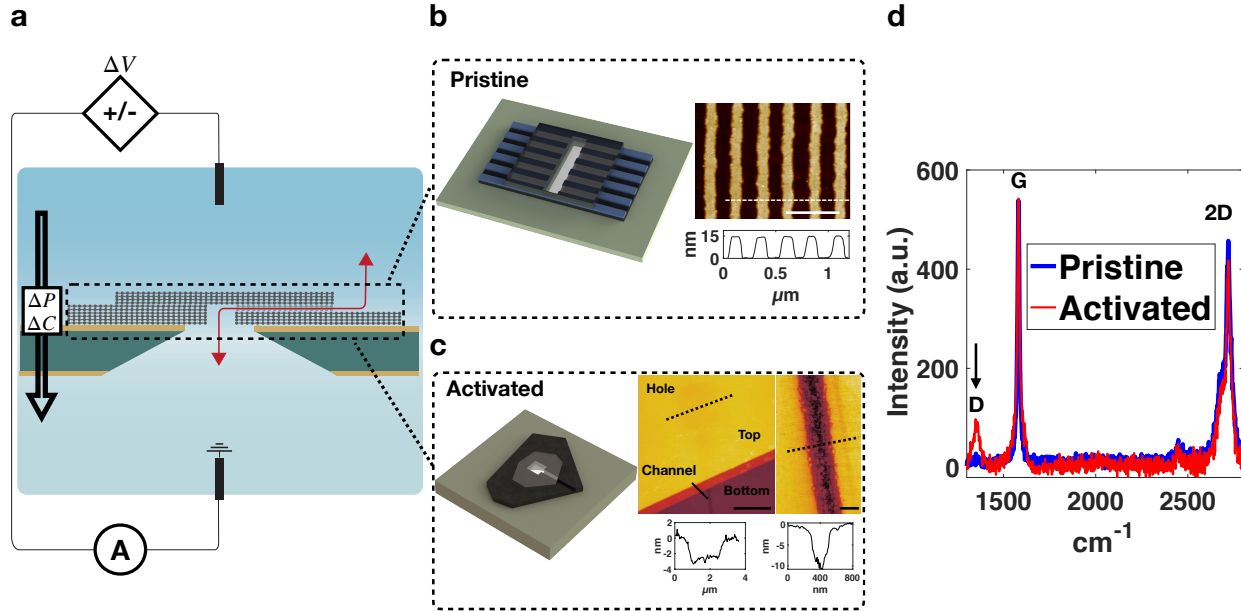


Figure2. Ionic transport across pristine and activated channels. Pristine channels: a, Ionic current under voltage drop, normalized per channel (System A: $N = 200$ channels, pH 5.5, thickness $h = 15$ nm). Inset: schematic cross sectional view of pristine nanochannels. b, Conductivity vs salt concentration at pH 5.5. Diamond points are experimental data. Solid black line represent the bulk theoretical conductivity. The red, solid and dashed, lines are the theoretical predictions for the conductivity using the electrokinetic framework building on Eq.(1). The solid red line assumes a scaling behavior $\Sigma(C_s) \propto C_s^{0.68}$, while the dashed red line corresponds to a constant surface potential prediction with $\Psi_0 = -50$ mV in Eq.(1); see text for details. All parameters for the concentration dependence of the surface charge and slip are summarized in the

Supplementary Information Section 4. c, Streaming current under pressure drop, normalized per channel, for various salt concentrations (pH5.5) d, Apparent zeta potential versus salt concentration (pH5.5). Diamond points are experimental data. The solid and dashed lines are the predictions for the apparent zeta potential using the surface charge scaling and constant surface potential, respectively, using same parameters as in panel b. **Activated channels:** a', Ionic current under voltage drop, normalized per channel (System E: $N=4$ channels, pH=5.5, thickness $h = 3$ nm). Inset: schematic cross section view of an activated nanochannel. b', Conductivity versus salt concentration. Solid circles are experimental data. Solid black line represent the bulk theoretical conductivity. The red solid and dashed lines are the predictions for the conductivity using the surface charge scaling ($\Sigma(C_s) \propto C_s^{0.32}$) and constant surface potential ($\Psi_0 = 240$ mV), respectively. Parameters for the concentration dependence of the surface charge and slip length are summarized in the Supplementary Information Section 4. c', Streaming current under pressure drop, normalized per channel, for various salt concentrations (pH5.5) d', Apparent zeta potential versus salt concentration (pH5.5). Solid circles are experimental data. The solid and dashed lines are the predictions for the apparent zeta potential using the surface charge scaling and constant surface potential, respectively, using same parameters as in panel b'. Error bars in panels d and d' are standard deviations from three and five measurements, respectively.

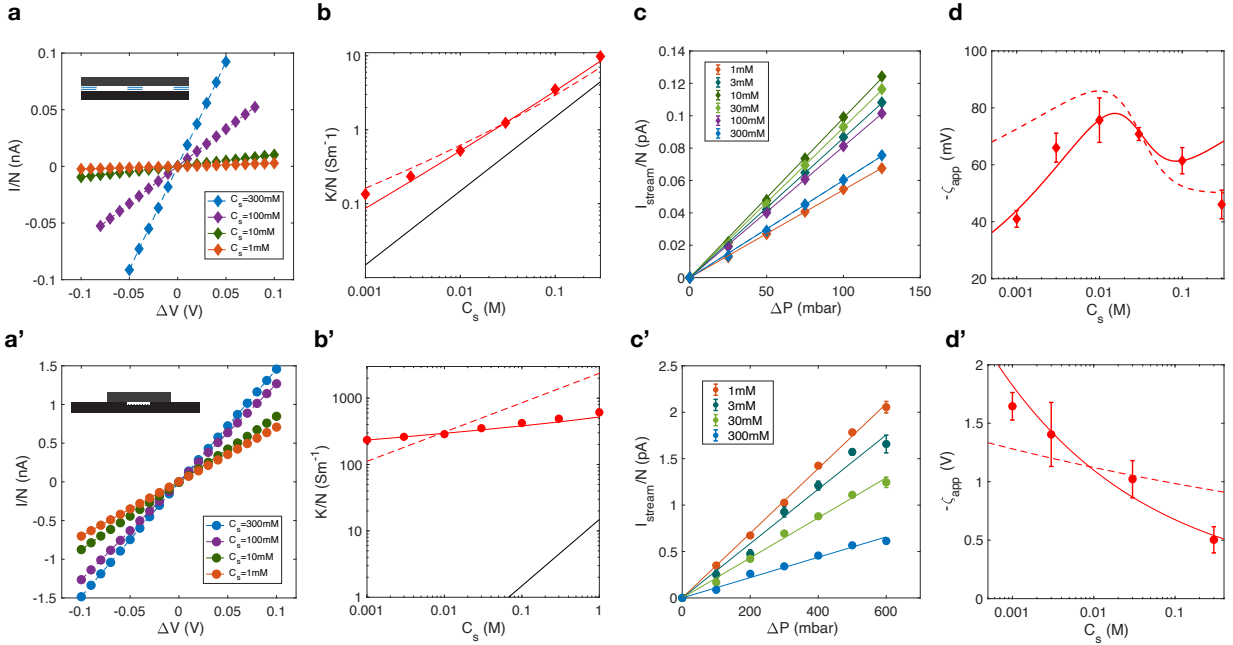


Figure3. Conductivity enhancement for pristine and activated channels: conductivity enhancement K/K_b versus concentration, with $K_b = 2e^2\mu C_s$ the bulk predicted conductivity (pH5.5). a, System B: pristine channel with thickness $h = 10$ nm, b, System A: pristine channel with thickness $h = 15$ nm, c, System F: channel with activated surface and thickness 8 nm, and d, System D: channel with activated

surface and thickness 10 nm. In all panels, points are experimental data and lines are the theoretical predictions for the conductivity enhancement using Eq.(1); see text. The solid red line assumes a scaling behavior $\Sigma(C_s) \propto C_s^\alpha$, while the dashed red line corresponds to the predictions assuming a constant surface potential Ψ_0 ; see text for details. For the pristine channels with 10 and 15 nm thickness, $\alpha = 0.62$ and $\alpha = 0.68$ respectively, while for the 8 and 10 nm activated channels, $\alpha = 0.33$, $\alpha = 0.40$ respectively. For the surface potential, we use $\Psi_0 = -0.025$ V and $\Psi_0 = -0.050$ V for the pristine channels (panel a and b, respectively), while results using $\Psi_0 = -0.220$ V, -0.210 V are shown for comparison for the 8 and 10 nm channels (panels c, d, respectively). All detailed parameters for the concentration dependence of the surface charge and slip are summarized in the Supplementary Information Section 4.

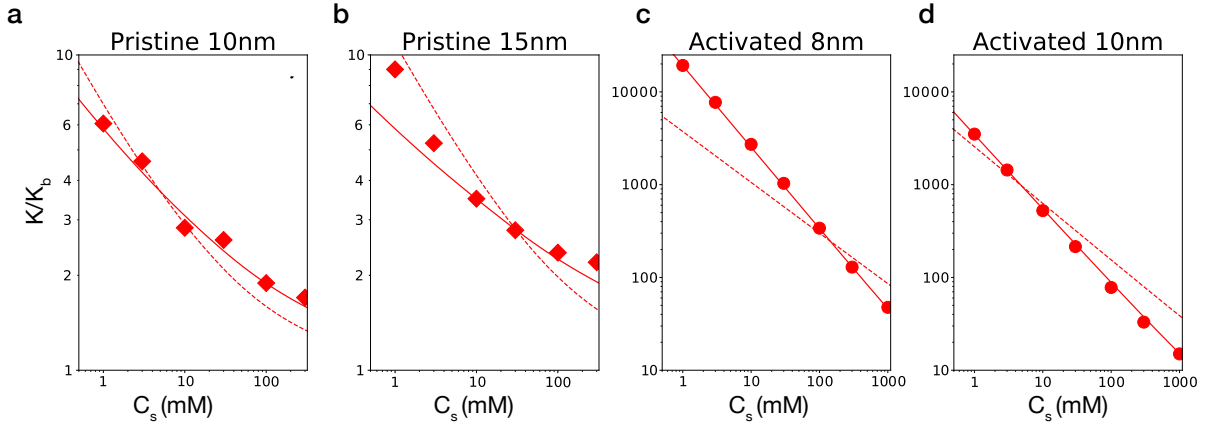
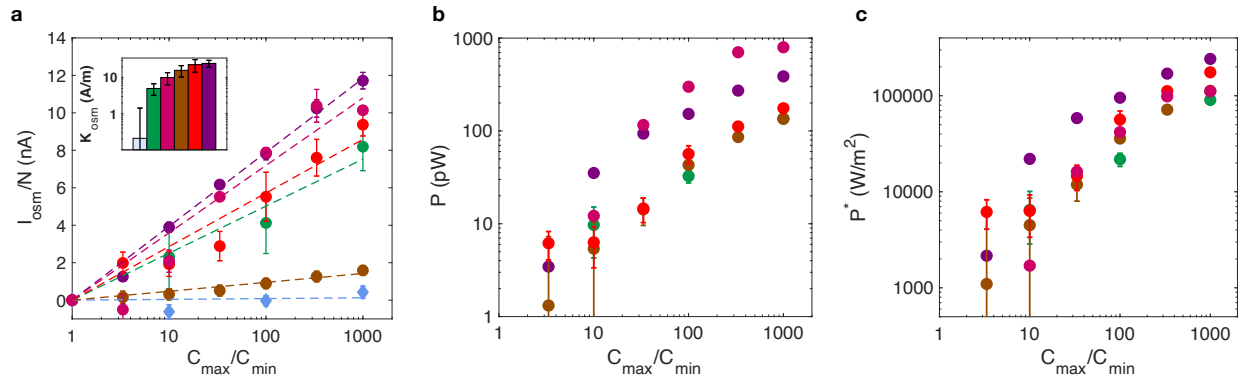


Figure4. Osmotic energy performance of pristine and activated channels. a, Osmotic current vs concentration ratio for a pristine channel (System C, blue color diamonds, with channel height 5 nm), and activated channels (System D (green color filled circles), System E (brown color filled circles), System F (purple color filled circles), System G (pink color filled circles) and system H (red color filled circles) with channel heights 10, 3, 5, 13 and 8 nm, respectively) (pH5.5). Measurements are performed by varying $C_{min} \in [1; 1000]$ mM, while keeping $C_{max} = 1$ M. Dashed lines are best linear fit. Inset : osmotic coefficient, K_{osm} of, from left to right, pristine (5 nm) and activated (10, 13, 3, 5, 8 nm) channels. Produced osmotic net power (b) and single pore power density (c) vs concentration ratio. Legend is the same as in panel a. Error bars in panels a, b and c are standard deviations from two different measurements at each concentration ratio.



-
- [1] Bocquet, L., Nanofluidics coming of age, *Nature Materials*, **19**, 254-256 (2020).
 - [2] S. Faucher, *et al.*, Critical knowledge gaps in mass transport through single-digit nanopores: a review and perspective, *Journal of Physical Chemistry C* **123**, 21309–21326 (2019).
 - [3] Kavokine, N., Netz, R. and Bocquet L., Fluids at the Nanoscale: From Continuum to Subcontinuum Transport *Annual Review of Fluid Mechanics*, **53**, 377-410 (2021).
 - [4] Radha, B., *et al.* , Molecular transport through capillaries made with atomic-scale precision, *Nature* **538**, 222-225 (2016).
 - [5] Nair, R.R., *et al.* , Unimpeded permeation of water through helium leak tight graphene-based membranes, *Science* **335**, 442-444 (2012).
 - [6] Ji, J., *et al.* Osmotic power generation with positively and negatively charged 2D nanofluidic membrane pairs, *Advanced Functional Materials*, **27**, 1603623 (2017).
 - [7] A., Jijo, *et al.* , Tunable sieving of ions using graphene oxide membranes, *Nature nanotechnology* **12.6**, 546 (2017).
 - [8] Yang, Q., *et al.* , Ultrathin graphene-based membrane with precise molecular sieving and ultrafast solvent permeation, *Nature materials* **16.12**, 1198-1202 (2017).
 - [9] Quan, X., Alibakhshi, M.A., Jiao, S., Xu, Z., Hempel, M., Kong, J., Park, H.G. and Duan, C., Fast water transport in graphene nanofluidic channels, *Nature Nanotechnology* **13**, 238-245 (2018).
 - [10] Ghanbari, H. and Esfandiari, A. , Ion transport through graphene oxide fibers as promising candidate

- for blue energy harvesting, *Carbon* **165**, 267-274 (2020).
- [11] Liu, X., He, M., Calvani, D., Qi, H., Gupta, K.B.S.S., de Groot, H.J., Sevink, G.A., Buda, F., Kaiser, U. and Schneider, G.F. , Power generation by reverse electrodialysis in a single-layer nanoporous membrane made from core–rim polycyclic aromatic hydrocarbons, *Nature Nanotechnology* **15** , 307-312 (2020).
- [12] Salanne, M., Rotenberg, B., Naoi, K. et al. Efficient storage mechanisms for building better supercapacitors, *Nature Energy* **1**, 16070 (2016).
- [13] Siria, A., Bocquet, M.-L. and Bocquet, L., New avenues for the large-scale harvesting of blue energy, *Nature Reviews Chemistry* **1**, 1-10 (2017).
- [14] Macha, M., Marion, S., Nandigana, V.V. and Radenovic, A., 2D materials as an emerging platform for nanopore-based power generation, *Nature Reviews Materials* **4.9**, 588-605 (2019).
- [15] Mouhat, F., Coudert, F.X. and Bocquet M.-L. , Structure and chemistry of graphene oxide in liquid water from first principles, *Nature Communications*, **11(1)**, 1-9 (2020).
- [16] Mouterde, T., Keerthi, A., Poggioli, A.R., Dar, S.A., Siria, A., Geim, A.K., Bocquet, L. and Radha, B., Molecular streaming and its voltage control in ångström-scale channels, *Nature* **567**, 87-90 (2019).
- [17] Ferrari, A.C. and Robertson, J. , Interpretation of Raman spectra of disordered and amorphous carbon, *Physical review B* **61(20)**, 14095 (2000).
- [18] Dresselhaus, M.S., Jorio, A. and Saito, R., Characterizing graphene, graphite, and carbon nanotubes by Raman spectroscopy, *Annu. Rev. Condens. Matter Phys.* **1(1)**, 89-10(2010).
- [19] M.Nakhara, Y. Sanada, Modification of pyrolytic graphite surface with plasma irradiation, *Journals of Materials science* **1(1)**, 1327-1333(1993).
- [20] Thiele, C., Felten, A., Echtermeyer, T.J., Ferrari, A.C., Casiraghi, C., Löhneysen, H.V. and Krupke, R. , Electron-beam-induced direct etching of graphene, *Carbon* **64**, 84-91 (2013).
- [21] Yuzvinsky, T.D., Fennimore, A.M., Mickelson, W., Esquivias, C. and Zettl, A. , Precision cutting of nanotubes with a low-energy electron beam, *Applied Physics Letters*, **86(5)**, 053109 (2005).
- [22] Levita, G., Restuccia, P. and Righi, M.C. , Graphene and MoS₂ interacting with water: A comparison by ab initio calculations, *Carbon*, **107**, 878-884 (2016).
- [23] J.L. Hueso, J.P. Espinosa, A. Caballero, J. Cotrino, A.R. Gonzalez-Elipe , XPS investigation of the reaction of carbon with NO, O₂, N₂ and H₂O plasmas *Carbon*, **45**, 89-96 (2007).
- [24] Grazia et al., Water at charged interfaces, *Nature Reviews Chemistry* **5**, 466-485 (2021)
- [25] Gopinadhan, K., Hu, S., Esfandiari, A., Lozada-Hidalgo, M., Wang, F.C., Yang, Q., Tyurnina, A.V., Keerthi, A., Radha, B. and Geim, A.K. , Complete steric exclusion of ions and proton transport through confined monolayer water, *Science* **363.6423**, 145-148 (2019).
- [26] Siria, A., Poncharal, P., Bianco, A.-L., Fulcrand, R., Blase, X., Purcell, S.T., and Bocquet, L., Giant osmotic energy conversion measured in a single transmembrane boron nitride nanotube, *Nature* **494**, 455-458. (2013).
- [27] Bocquet, L., & Charlaix, E., Nanofluidics, from bulk to interfaces, *Chemical Society Reviews* **39.3**,

- 1073-1095 (2010).
- [28] Grosjean, B., Bocquet, M. L., Vuilleumier, R., Versatile electrification of two-dimensional nanomaterials in water, *Nature communications*, **10**, 1-8 (2019).
- [29] Secchi, E., Niguès, A., Jubin, L., Siria, A. and Bocquet, L., Scaling behavior for ionic transport and its fluctuations in individual carbon nanotubes, *Physical Review Letters* **116.15**, 154501 (2016).
- [30] T. Mouterde and L. Bocquet, Interfacial transport with mobile surface charges and consequences for ionic transport in carbon nanotubes, *European physical journal. E*, **41**, 148 (2018).
- [31] S.R. Maduar, A.V. Belyaev, V. Lobaskin, and O.I. Vinogradova, Electrohydrodynamics Near Hydrophobic Surfaces, *Phys. Rev. Lett.* **114**, 118301 (2015).
- [32] Manghi, M.; Palmeri, J.; Yazda, K.; Henn, F.; Jourdain, V., Role of Charge Regulation and Flow Slip on the Ionic Conductance of Nanopores: an Analytical Approach, *Physical Review E*, **98**, 012605 (2018).
- [33] Biesheuvel, P. M., Bazant, M. Z. Analysis of Ionic Conductance of Carbon Nanotubes, *Physical Review E* **94**, 050601 (2016).
- [34] Uematsu, Y., Netz, R. R., Bocquet, L. and Bonthuis, D.J., Crossover of the Power-Law Exponent for Carbon Nanotube Conductivity as a Function of Salinity, *J. Phys. Chem. B*, **122**, 2992-2997 (2018).
- [35] Joly, L., Ybert, C., Trizac, E. and Bocquet, L., Liquid friction on charged surfaces: From hydrodynamic slippage to electrokinetics, *J. Chem. Phys.* **125**, 204716 (2006).
- [36] Xie, Y., Fu, L., Niehaus, T., and Joly, L., Liquid-Solid Slip on Charged Walls: The Dramatic Impact of Charge Distribution *Phys. Rev. Lett.* **125**, 014501 (2020).
- [37] Squires, T. M., Electrokinetic flows over inhomogeneously slipping surfaces, *Physics of Fluids* , **20(9)**, 092105 (2008).
- [38] Jiandong, F., Graf, M., Liu, K., Ovchinnikov, D., Dumcenco, D., Heiranian, M., Nandigana, V., Aluru, N.R., Kis, A. and Radenovic, A., Single-layer MoS2 nanopores as nanopower generators, *Nature* **536**, 197-200 (2016).
- [39] Lin, C. -Y., Combs, C., Su, Y. -S., Yeh, L. -H. and Siwy, S., Rectification of Concentration Polarization in Mesopores Leads To High Conductance Ionic Diodes and High Performance Osmotic Power, *Journal of the American Chemical Society* **141**, 3691-3698 (2019).
- [40] Ma, T., Balanzat, E., Janot, J. -M. and Blame, S., Nanopore Functionalized by Highly Charged Hydrogels for Osmotic Energy Harvesting, *ACS Applied Materials & Interfaces* **11**, 12578-12585 (2019).
- [41] Gao, M., Tsai, P. -C., Su, Y. -S., Peng, P.-H., and Yeh, L. -H., Single Mesopores with High Surface Charges as Ultrahigh Performance Osmotic Power Generators, *Small* **16**, 2006013 (2020).
- [42] Xiao, F. et al., A general strategy to simulate osmotic energy conversion in multi-pore nanofluidic systems, *Materials Chemistry Frontiers* **2**, 935-941 (2018).
- [43] Gao, J., Liu, X., Jiang, Y., Ding, L., Jiang, L. and Guo, W., Understanding the Giant Gap between Single-Pore- and Membrane-Based Nanofluidic Osmotic Power Generators, *Small* **215**, 1804279 (2019).
- [44] Fumagalli, L., et al. , Anomalously low dielectric constant of confined water, *Science* **360.6395**, 1339-

1342 (2018).

Methods

Fabrication of pristine nanochannel devices. Pristine graphene nanochannels, Fig. 1b, are prepared as in Refs.[4, 25, 44]. Briefly, a single crystal of known thickness is patterned using ebeam lithography (EBL) and etched using dry etching to form an array of strips (spacer layer). This spacer layer is used to separate two graphite crystals (top and bottom layers) of thickness between 70 to 100 nm using vdW assembly. The channels consists of the free space remaining between the strips (Fig.2a). Fluidic device with 'activated' carbon nanochannels (Fig. 1c) is fabricated by etching the nanochannel in a bottom crystal of 50 to 100 nm. The bottom is then covered by a top layer of similar thickness.

Fabrication of activated nanochannel devices. Two different nano-fabrication processes are used to fabricate the activated nanochannels. In the first method the channel are etched in an H₂O reactive environment inside a Scanning Electron Microscope (SEM) while in the second, the channels are etched in O₂ using Reactive Ion Etching (RIE).

For the H₂O-etched channels, first, we created a square-shaped aperture ($1\ \mu\text{m} \times 1\ \mu\text{m}$), see Supplementary Fig. 1, on the bottom layer graphite crystal by completely etching through it *via* electron beam induced direct etching (EBIE) in a water vapor environment inside a SEM [20]. Using the same method, a trench of few micrometers length and, channel height varied between 3 and 13 nm is made from one end of the square-shaped aperture by making sure the trench and the aperture are connected. We then placed a top layer graphite crystal on the patterned bottom layer using vdW assembly to fabricate the activated nanochannel. This whole assembly prepared on SiO₂/Si substrate is finally transferred onto a Silicon Nitride (SiN_x) membrane with a circular aperture of diameter $10\ \mu\text{m}$. (see Supplementary Information, section 1).

For the O₂ etched channels, a bottom layer graphite is first transferred onto the silicon nitride membrane with a rectangular hole of $3\ \mu\text{m} \times 20\ \mu\text{m}$. Then, the rectangular hole in SiN_x membrane is extended into the bottom layer using oxygen plasma dry etching in RIE from the backside of the Si/SiN_x wafer. Subsequently, the bottom layer is patterned using e-beam lithography and oxygen plasma dry etching in RIE to create a single channel. Finally, a graphite crystal is transferred on top of this patterned bottom layer with single channel to obtain the nanochannel device for our experiments. Graphite crystals used in this work to fabricate fluidic devices with pristine and activated nanochannels are obtained by mechanical exfoliation.

Ionic conductivity, streaming and osmotic current measurements. Ionic current measurements under various driving forces are performed by clamping the nanofluidic devices between two reservoirs as described in [4, 26]. These reservoirs are filled with potassium chloride (KCl) solutions with concentration C_s varying between 1 mM and 1 M; pH is also varied between 3 and 9. Silver Chloride (Ag/AgCl)

electrodes placed in the reservoirs are used for electrical current measurements and voltage drop application. They are connected to a patch clamp amplifier (*Molecular Devices Axopatch 200B*). First, the response to voltage drop and pressure drop is measured. Voltage drop between -100 mV and 100 mV is applied with 5 seconds steps of 10 mV. The last current value of each step is recorded. The pressure is applied with a pump connected to the channel's side reservoir with an integration time of typically 15-100 s (see Supplementary Information Section 3.2). Osmotic current measurements are performed by filling each of the reservoir with solutions of different KCl concentration. Specifically, the reservoir connected to the channel is filled with a 1 M KCl solution while the other side is loaded with solution with concentration 10^{-3} M-1 M (see Supplementary Information Section 3.3). All measurements are sampled at 1 kHz with an acquisition time set to 0.1 s.

Data Availability

The data supporting the findings of this study are available within the paper and its Supplementary Information files. Raw data are provided as Source data and in <https://figshare.com/s/2aabcab85d33123a3af3>.